Catalysis Today 437 (2024) 114783

Contents lists available at ScienceDirect

Catalysis Today

journal homepage: www.elsevier.com/locate/cattod

Photoelectrochemical disinfection efficiency of WO_3-based photoanodes: Development of multifunctional photoelectrocatalytic materials

Conor Reddick [a,b], Carlos Sotelo-Vazquez [a], Brian Tam [c], Andreas Kafizas [c,d], Ken Reynolds [b], Simon Stanley [b], George Creasey [c,e], Anna Hankin [c,e], Cristina Pablos [a,*], Javier Marugán [a,f]

[a] Chemical and Environmental Engineering Group, ESCET, Universidad Rey Juan Carlos, C/Tulipán s/n, Móstoles, Madrid 28933, Spain
[b] ProPhotonix IRL Ltd., 3020 Euro Business Park, Little Island, Cork T45 X211, Ireland
[c] Department of Chemistry, Molecular Science Research Hub, Imperial College London, London W12 0BZ, UK
[d] Grantham Institute for Climate Change and the Environment and The London Centre for Nanotechnology, Imperial College London, London SW7 2AZ, UK
[e] Department of Chemical Engineering, Imperial College London, South Kensington Campus, SW7 2AZ, UK
[f] Instituto de Investigación de Tecnologías para la Sostenibilidad. Universidad Rey Juan Carlos, C/Tulipán s/n, Móstoles, Madrid 28933, Spain

ARTICLE INFO

Keywords:
E. coli
MS2 virus
Water treatment
Heterojunction
Nanostructure

ABSTRACT

Access to safe water is a growing global concern, with millions lacking acceptable water sources. Photocatalysis offers eco-friendly water remediation, yet its combination with electrocatalysis for both water treatment and hydrogen production remain underexplored. This study investigates UVA LED photoelectrocatalysis using WO_3-based photoanodes, alone or in heterojunction with $BiVO_4$, to purify wastewater and co-produce hydrogen. Tests on polluted water streams containing 10^5 PFU mL^{-1} of MS2 bacteriophage virus and 10^6 CFU mL^{-1} of *E. coli* reveal that nanostructured WO_3 achieves rapid MS2 disinfection within 5 min. ($k = 0.80\ min^{-1}$), with enhanced efficiency over flat counterparts. However, nanostructuring does not improve *E. coli* inactivation due to bacterium size constraints. These findings advance the design of tandem photoreactors for dual wastewater purification and energy generation.

1. Introduction

The presence of bacteria and viruses in wastewater, especially following the SARS, MERS, and SARS-CoV-2 pandemics, has raised global health concerns. These pathogens, resilient to environmental conditions, are responsible for waterborne diseases [1]. Traditional wastewater treatments like chlorination and ozonation have been standard, but recent concerns have arisen due to their potential to generate carcinogenic disinfection by-products [2]. With climate change exacerbating water scarcity, the demand for innovative tertiary water treatment methods is pressing, especially amidst the growing reliance on treated wastewater reuse [3–5].

Advanced Oxidation Processes (AOP), which use photocatalysts to generate *in-situ* highly reactive transitory species capable of converting organic contaminants to harmless by-products, have been explored as alternatives. Inorganic semiconductor systems like TiO_2, ZnO, CuO, and WO_3 are commonly used for their stability and low toxicity. However, these photocatalysts require long-lived photogenerated charge carriers to oxidise water contaminants efficiently [6]. Strategies to minimise charge carrier recombination have been explored, being the formation of heterojunction systems, such as anatase/rutile TiO_2, Cu_2O/TiO_2, WO_3/TiO_2, and $WO_3/BiVO_4$, the most effective method to improve charge transport and reduce their recombination [7–11]. Additionally, nanostructuring of heterojunction systems can greatly improve photocatalytic efficiency by separating long light absorption depths and inadequate minority carrier diffusion lengths to enhance charge carrier transport [11–14].

In this work, we investigate the efficiency of flat and nanostructured WO_3, and their combinations with $BiVO_4$, to eliminate water contaminants using electrocatalysis (EC), photocatalysis (PC), and photoelectrocatalysis (PEC). Previous research has shown that the inactivation of MS2 and *E. coli* under PEC conditions can be achieved using various photocatalytic materials, including TiO_2 [15-17] and WO_3 [18,19]. However, some research groups have found that the choice of supporting electrolyte for inactivation experiments can significantly impact the formation of reactive species and the subsequent photocatalytic efficiency. McMichael *et al.* tested TiO_2 nanotubes with NaCl and Na_2SO_4 electrolytes for PEC inactivation of *E. coli* K12 [16], finding that NaCl led

---

* Corresponding author.
E-mail address: cristina.pablos@urjc.es (C. Pablos).

https://doi.org/10.1016/j.cattod.2024.114783
Received 18 November 2023; Received in revised form 25 April 2024; Accepted 29 April 2024

to rapid *E. coli* inactivation (5- log (99.999 %)) in 30 min, whilst Na_2SO_4 achieved a 2.51- log (99.61 %) reduction in 180 min. This difference was attributed to the generation of reactive chlorine species in NaCl that were able to contribute to the break down of the bacterium.

Nanostructured WO_3 photoanodes have shown remarkable inactivation rates for both MS2 and *E. coli*. Tolosana-Moranchel *et al.* compared WO_3 and P25 photoanodes, observing that WO_3 achieved 5-log (99.999 %) inactivation of MS2 (initial concentration 10^7 PFU mL^{-1}) in 6 min compared to 5- log (99.999 %) inactivation within 14 min when P25 was used (1.3 V vs SCE, solar simulator). The higher efficiency of WO_3 was explained in terms of its morphology, which presented a higher ratio of absorbed radiation to incident radiation for their radiation source and reduced electron-hole recombination [18]. Additionally, coupling WO_3 with metal oxides like $BiVO_4$ can produce highly efficient photocatalytic systems, which have been historically used for energy storage applications [20]. However, some work in water remediation has been conducted with $WO_3/BiVO_4$ systems. Cristino *et al.* studied the removal of contaminants of emerging concern ketoprofen and levofloxacine [21], finding that both contaminants were oxidised at the $WO_3/BiVO_4$ interface faster than their single analogues. Another study conducted by Omrani *et al.* was based on the photocatalytic degradation of sulfasalazine using nano-composite WO_3 and $WO_3/BiVO_4$, finding a near four-fold improvement in removal efficiency for the heterojunction system [22]. However, despite the wide use of these heterojunction systems for energy storage applications, there is a lack of research on the use of $WO_3/BiVO_4$ and PEC for water remediation applications.

In this work, we evaluate the implementation of five different photocatalytic materials (flat and nanostructured WO_3, flat $BiVO_4$, as well as flat and nanostructured $WO_3/BiVO_4$) for PEC water treatment applications by studying their kinetics and energy efficiency for the removal of model organic (methanol, MeOH), bacterial (*E. coli*) and viral (MS2) species. To understand the impact of voltage bias and light, samples herein are examined with/ without voltage bias (*i.e.* under PEC and PC conditions) and with/ without light (*i.e.* under PEC and EC conditions). The primary aim of this work is to identify the materials and parameters that result in the most effective PEC disinfection of water streams. As hydrogen is co-evolved during PEC operation, the outcomes of this work represent a step forward in the development of multifunctional materials for water treatment and energy storage applications.

2. Experimental

2.1. Photoanode materials

Flat and nanostructured WO_3, $BiVO_4$, and layered heterojunction systems were synthesised *via* aerosol-assisted chemical vapour deposition (AACVD). The photocatalytic materials were deposited onto fluorine-doped tin oxide (FTO) substrates (1.25 ×2.5 cm, TEC 15, Hartford Glass Co.), with the photocatalyst layer covering 2.5 cm^2. The synthesis of WO_3 was previously reported by Kafizas et al [23]. The same method was used here for the WO_3 and adapted for the synthesis of $BiVO_4$ by AACVD. Triphenyl bismuth (Alfa Aesar, 98 %) and vanadium (III) acetylacetonate (Aldrich, 97 %) were dissolved in a 3:1 solution of acetone:methanol and transferred with compressed air carrier gas at a flow rate of 1 L min^{-1} over a substrate heated at 400 °C.

2.2. Physical characterisation

The physical characterisation of flat and nanostructured WO_3 was previously reported by Kafizas *et al.* [23]. In this work, X-ray diffraction (XRD) patterns were measured on a modified Bruker-AXS D8 diffractometer with parallel beam optics equipped with a PSD LynxEye silicon strip detector. X-rays were generated using a Cu source ($V = 40$ kV, $I = 30$ mA) with Cu $K_{\alpha1}$ ($\lambda = 1.54056$ Å) and Cu $K_{\alpha2}$ ($\lambda = 1.54439$ Å) emitted with an intensity of 2:1. The incident beam was held at 1° with respect to the sample and the angular range of the patterns collected between $6^\circ \leq 2\Theta \leq 70^\circ$ with a step size of 0.034°. The patterns were compared with standards from the Physical Sciences Data-Service, confirming the deposition of $BiVO_4$ on the FTO and on WO_3 when fabricating heterojunctions as shown in the Supplementary Information Figure S1. The morphology and thicknesses of the WO_3 and $BiVO_4$ films were studied using a Zeiss Auriga Cross Beam instrument (5 kV, working distance 5.0 nm). To prevent charging, the samples were sputter-coated with a thin layer of chromium (~15 nm). All SEM images of the samples used in this work are shown in the Supplementary Information Figure S4. For the samples tested in this work, the flat WO_3 samples had thicknesses of approximately 400 nm, while the flat $BiVO_4$ formed with thicknesses of 200 nm. The flat $WO_3/BiVO_4$ has a 400 nm thick layer of WO_3 and a 400 nm thick layer of $BiVO_4$. The nanostructured WO_3 formed a layer 2000 nm thick and the $BiVO_4$ uniformly coats the WO_3 nanoneedles with a radial thickness of 50–100 nm. Transmission electro microscopy (TEM) images of WO_3 nanoneedles and $WO_3/BiVO_4$ NNS heterojunctions were analysed using a JEOL 2100Plus instrument with Gatan Digital Micrograph software. All TEM and STEM images are shown in the Supplementary Information (Figures S5, S6, and S7). Optical properties and bandgap measurements are shown in Figure S8. Additionally, X-ray photoelectron spectroscopy (XPS) analyses (Figure S9 and S10) were performed using a Thermo Scientific K-alpha spectrometer with monochromated Al K alpha radiation, a dual beam change compensation system and constant pass energy of 50 eV. Survey scans were collected in the range of 0–1200 eV. High-resolution peaks were used for the principal peaks of W (4 f), Bi (4 f), V (2p), O (1 s), and C (1 s), which were modelled using sensitivity factors to study the environment of the different elements within the region of analysis (spot size 400 nm).

2.3. Photoelectrochemical cell setup

The experiments were conducted using a solution of 0.1 M Na_2SO_4 and deionised water, sterilised in an autoclave at 121 °C for 21 min. They were carried out in a 50 mL borosilicate cell with a jacket, illuminated by a digitally controlled UVA LED Lamp (365 nm +/- 5 nm at 25 ºC, Seoul Viosys UV1000–36, emission range 343 – 400 nm) placed above the cell. A full description of the UVA LED lamp used in this paper can be found elsewhere [24]. The UVA lamp was chosen to provide photons of sufficient energy to photoexcite electrons in both the WO_3 and $BiVO_4$ materials. The cell has a 1.5 × 2.5 cm opening in its lid to allow light in and was covered by an opaque jacket to prevent light ingress from external sources. The solution was stirred continuously at 200 rpm by a magnetic PTFE stir bar to keep the pollutants evenly distributed. A three-electrode setup was used for photoelectrochemical and electrochemical experiments, with a back-lit photoanode, an Ag/AgCl reference electrode (0.197 V NHE at 298 K, eDAQ), and a platinum mesh counter electrode (2 × 2 cm). To ensure a high degree of photon absorption close to the TCO/photocatalyst interface, irradiation was performed from the back side. The thicker materials are nanostructured allowing for improved migration of charge carriers to the surface. Additionally, the nanostructured photoanodes are porous allowing diffusion of pollutants into the structure. The mesh platinum counterelectrode used in the work reduced the number of photons reaching the photoanode surface significantly, thus choosing back lit conditions would maximise photons reaching the photoanode and being absorbed close to the TCO/photocatalyst surface to reduce charge carrier recombination.

The photoanode and counter electrode were 1.5 cm apart and controlled and monitored by an Autolab potentiostat (μAutolab Type III). Images of the experimental setup can be found in the Supplementary Information (Figure S3). The radiant intensity from the lamp in the cell was determined by ferrioxalate actinometry [25], also shown in the Supplementary Information (Figure S4). Two UVA LED based radiant intensity values were used in this work, 44.7 mW cm^{-2} ± 1.19 mW cm^{-2} for methanol oxidation and MS2 inactivation, whilst 19.1 mW cm^{-2} ± 1.35 mW cm^{-2} was used for *E. coli* inactivation, as it was found from initial tests that the higher radiant intensity value achieved a 5-log (99.999 %) reduction of the *E. coli* within one hour, and thus would be unsuitable to assess the inactivation kinetics of the photocatalytic materials. Tests were conducted under photoelectrocatalytic (UVA lamp on, potential bias applied in closed circuit), electrocatalytic (UVA lamp off, potential bias applied in closed circuit), and photocatalytic (UVA lamp on, no potential bias applied in open circuit). PEC, EC, and PC experiments were repeated in triplicate, with the mean and standard deviation calculated to represent the average and error values, respectively.

2.4. MS2 enumeration

MS2 coliphage (ATCC 15597B1) was used as a model virus for evaluating disinfection kinetics. The inactivation of viable MS2 virus was determined by a double-layer agar method, requiring Tryptone Yeast Glucose (TYG) medium, semi-solid agar, and agar. TYG medium was prepared using 10 g L^{-1} tryptone (vegetable, Millipore), 1 g L^{-1} yeast extract (Sigma-Aldrich), and 8 g L^{-1} NaCl in deionised water. Additionally, 5 g L^{-1} and 15 g L^{-1} of agar (Sigma-Aldrich) were added to the medium to prepare semi-solid and solid agar medium, respectively. All solutions were autoclaved at 121 °C for 21 min, after which 10 g L^{-1} glucose (Sigma Life Sciences), 2.94 g L^{-1} $CaCl_2$ (Sigma-Aldrich), and 0.01 g L^{-1} thiamine (sigma-Aldrich) were added to the solutions when cooled to 50 ºC. The bacterial host (*E. coli* C300 171, ATCC 15597) was cultured in TYG medium for 6 h at 37 ºC with rotary agitation of 100 rpm prior to enumeration. 1 mL of the bacterial host was then mixed with 0.1 mL of sample (or decimal dilutions using Phosphate Buffer Saline) and 5 mL of melted semi-solid TYG agar. The mixture was then poured onto 100 mm of solid TYG agar dishes and left to air dry in a biological safety cabinet. Solidified plates were inverted and incubated at 37 ºC for 24 h before examining for plaques. The detection limit of this method was 2 PFU mL^{-1}. An initial MS2 concentration of 10^5 PFU mL^{-1} was used during inactivation experiments.

2.5. E. coli enumeration

E. coli K-12 (ATCC 23631) was used as a model bacterium for evaluating the inactivation kinetics. *E. coli* was cultured overnight in Luria Bertani broth (tryptone 10 g L^{-1}, NaCl 10 g L^{-1} and yeast extract 5 g L^{-1}, Sigma-Aldrich) and incubated at 37 ºC, with rotatory agitation of 100 rpm under aerobic conditions. Bacteria were collected after 20–24 h of incubation, yielding a concentration of 10^8 CFU mL^{-1}. 1 mL of *E. coli* suspensions was centrifugated at 3500 rpm for 25 min, washed three times with 0.1 M Na_2SO_4 solution and diluted to 10^6 CFU mL^{-1}. The bacterial inactivation was followed by analysing the concentration of viable bacteria in the samples taken throughout the reaction. The quantification was carried out following a standard serial dilution procedure, spotting 10 μl samples of each decimal dilution on 100 mm LB nutrient agar plates and incubating them at 37 ºC for 24 h before counting. For reaction times with lower bacteria concentrations, higher volumes (100 mL and 1 mL) of the undiluted suspensions were also plated to reduce the detection limit to 10 CFU mL^{-1}. *E. coli* initial concentrations were 10^6 CFU mL^{-1}.

2.6. Formaldehyde colorimetry

Methanol was chosen as a model organic pollutant to evaluate the degradation of organic matter. The experimental setup consisted of a supporting electrolyte solution of 0.1 M Na_2SO_4 (Scharlau) containing methanol (Scharlau) with an initial concentration of 0.1 M. Given that methanol is in excess and dissolved oxygen is present in the reaction solution, methanol is selectively oxidised to formaldehyde. Given the excess of methanol in the system, the system can be described by a zero-order kinetic model, as demonstrated previously [26,27]. Thus, the evolution of formaldehyde was followed through Nash's colourimetric method [25].

2.7. Electrochemical characterisation

Linear sweep voltammetry was conducted on all photoanodes, as well as the blank FTO substrate, for all pollutants in a solution of 0.1 M Na_2SO_4 in darkness and light at a sweep rate of 50 mV s^{-1} between 0.35 and 1.50 V vs Ag/ AgCl During EC and PEC reactions, chronoamperograms were recorded at a +0.5 V vs Ag/AgCl potential bias. A UVA LED light intensity of 44.7 mW cm^{-2} ± 1.19 mW cm^{-2} was used for all voltammetry tests regardless of the enhanced inactivation of *E. coli* at this light intensity to compare the photocurrent response between all three pollutants under equivalent conditions.

2.8. Faradaic efficiency calculation

The Faradaic efficiencies of the photoanodes were calculated from the MeOH oxidation experiments, as the known stoichiometry of the conversion of methanol to formaldehyde gives a more accurate value than the calculation using the approximate number of hydroxyl radicals involved in the inactivation of MS2 and *E. coli*. A two-step methanol oxidation mechanism has been previously proposed, where the reaction begins with the adsorption of the methanol molecule to a metal centre, releasing a proton. Then, a surface hole is transferred to the methoxide forming a methoxy radical, which then undergoes a second oxidation step when an electron is injected into the conduction band of the photoanode, producing formaldehyde [28–30]. The proposed mechanism is shown below:

$$OH^- + h^+ \rightarrow OH\cdot$$

$$OH\cdot + CH_3OH \rightarrow \cdot CH_2OH + H_2O$$

$$\cdot CH_2OH + OH^- \rightarrow HCHO + H_2O + e^-$$

The Faradaic efficiency was calculated by dividing the measured rate of formaldehyde generated by the photocurrent generated from all reactions in the cell [31]:

$$FE(\%) = \frac{CH_2O(mols^{-1}) \quad \times \quad N_A}{(I_{Photo})/e} \tag{1}$$

Where CH_2O is the rate of formation of formaldehyde in the reaction, N_A is the Avogadro's number, I_{Photo} is the average photocurrent per second during the formaldehyde formation reaction, and e is the elementary charge constant.

3. Results and discussion

3.1. Linear sweep voltammetry; PEC and EC performance

The current-voltage characteristics of the WO_3 and $BiVO_4$ photoanodes were analysed by linear sweep voltammetry, as shown in Fig. 1. All photoanodes containing WO_3 produced photocurrent under irradiation across the tested voltage range for all pollutants examined. It should be noted that under the testing conditions employed there will be competition between the oxidation of water and the pollutant. Importantly, the intermediates that can be formed during the oxidation of water (e.g. hydroxyl radicals, hydrogen peroxide, etc.) may contribute to the indirect oxidation of the pollutants present.

In darkness, an onset in the current was seen at a potential of roughly 1.4–1.45 V vs Ag/AgCl, which is typical for these photoanode materials [32]. Under irradiation, flat $BiVO_4$ presented an onset potential for all solutions of ~1 V vs Ag/AgCl, whereas all WO_3 and $WO_3/BiVO_4$ materials presented onset potentials of 0.4 V vs Ag/AgCl or less. The positive shift in the onset potential of the flat $BiVO_4$ photoanode is likely caused by the dead layer effect. This effect arises due to the thin layer of $BiVO_4$

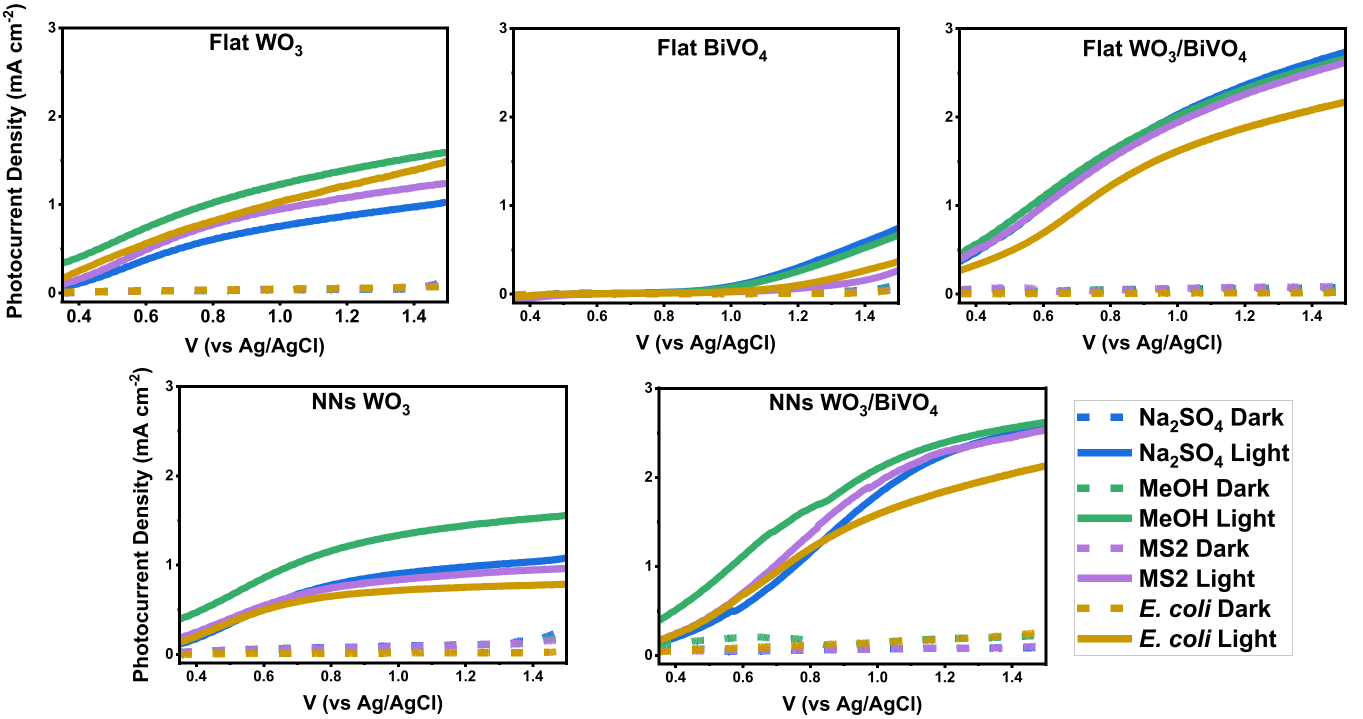

Fig. 1. Current–voltage curves of select photoanodes measured in 0.1 M Na_2SO_4 electrolyte (pH = 6.38), in a mixture of 0.1 M Na_2SO_4 with 0.1 M MeOH, and in a mixture of 10^5 PFU mL^{-1} with 0.1 M Na_2SO_4 for dark (dashed lines) and back irradiation (solid lines) conditions. Photoanodes were irradiated from the back using a 365 nm LED light. The voltage was swept from the cathodic to anodic potentials from 0.35 to 1.5 V_{RHE} (50 mV s^{-1}).

deposited on FTO [33] (shown in the inset of Figure S2(c) of Supplementary Information). It is believed that this mismatch in lattice morphology between the $BiVO_4$ and FTO leads to the formation of amorphous material close to the interface dense in trap sites [34]. Flat and nanostructured WO_3 materials provide the greatest improvements in photocurrent with the introduction of methanol to the sodium sulphate electrolyte, with methanol acting as a hole scavenger to reduce recombination [35]. Interestingly, the introduction of methanol to the sodium sulphate solution results in a large increase in photocurrent for NNs WO_3, however a lesser increase is observed for NNs $WO_3/BiVO_4$ as the valance band holes of the $BiVO_4$ layer have lower energy than WO_3 to generate hydroxyl radicals from water for methanol oxidation [36,37]. Another explanation could be that the electron-hole pairs in the $WO_3/BiVO_4$ heterojunction materials are much longer lived than in WO_3 materials, which increase the rate of water oxidation, a typically slow reaction requiring holes to exist for relatively long periods of time [38,39]. Another factor is differences in concentration, with water being ~550 parts per 1 part of methanol. Therefore, the introduction of methanol to the cell would not be expected to drastically increase the photocurrent produced. Across the range of materials, the voltammetry tests with 10^6 CFU mL^{-1} *E. coli* partially reduced the photocurrent produced compared to the 0.1 M Na_2SO_4 alone. The reduction in photocurrent could be attributed to the large size of *E. coli* bodies blocking sites on the photocatalytic material, a steric hindrance effect, thus reducing the production rate of oxidating species [40,41]. Similarly, voltammetry measurements with 10^5 PFU mL^{-1} MS2 reduced the photocurrent compared to 0.1 M Na_2SO_4 solutions but to a lesser extent compared to *E. coli*, likely due to the smaller size and lower concentration of MS2 in solution blocking less sites on the photocatalytic surface than *E. coli*.

3.2. Evaluation of the methanol oxidation performance

For reactions including MeOH, the efficiency of MeOH oxidation to formaldehyde was assessed. For PEC and EC tests, samples were held at an applied potential of 0.5 V vs Ag/ AgCl. For PEC and PC tests, samples were irradiated with a 365 nm UVA LED light.

Fig. 2 shows the PEC, EC and PC kinetic constants for the oxidation of methanol to formaldehyde. Plots of formaldehyde formation *versus* time are shown in Supplementary Information (Figure S5). PEC kinetic constants were at least one order of magnitude higher than those found under EC and PC conditions.

When used alone, $BiVO_4$ suffers from high electron-hole recombination due to the short diffusion lengths of the charge carriers (~70 nm) [42]. However, when coupled in a heterojunction with WO_3, charge carrier diffusion is improved by the offset in band energies and induced electric fields [20]. Higher kinetic constants were seen for nanostructured materials compared to their flat equivalents, which was attributed to the combination of increased material thickness (allowing for higher photon absorption), an increased active surface area available for MeOH oxidation, and a shorter diffusion path through the nanostructured WO_3 for the charge carriers formed [43]. Comparing the nanostructured materials in more detail, the $WO_3/BiVO_4$ sample showed a lower kinetic constant for MeOH oxidation to formaldehyde than the WO_3 sample (Fig. 2). This was despite the photocurrent being partly higher in the nanostructured $WO_3/BiVO_4$ sample (Fig. 1). This is attributed to the comparatively lower Faradaic efficiency (calculated from Eq. 1) seen in nanostructured $WO_3/BiVO_4$ for MeOH oxidation to formaldehyde (~62 %) compared with nanostructured WO_3 (~100 %). The cause of this lower Faradaic efficiency may be due to changes in selectivity, where a greater preference for water oxidation and/or alternative MeOH oxidation products may be present in the nanostructured $WO_3/BiVO_4$ sample. It should be noted that the near-zero photocurrent measurements and low formaldehyde production rates for MeOH oxidation on flat $BiVO_4$ photoanodes gave Faradaic efficiencies with error values greater than 100 %, and therefore, were not included.

In ascending order, the Faradaic efficiencies (shown in Fig. 2) of the photoanodes are flat $WO_3/BiVO_4$ < flat WO_3 < NNs $WO_3/BiVO_4$ < NNs WO_3. Interestingly, these Faradaic efficiencies closely followed the

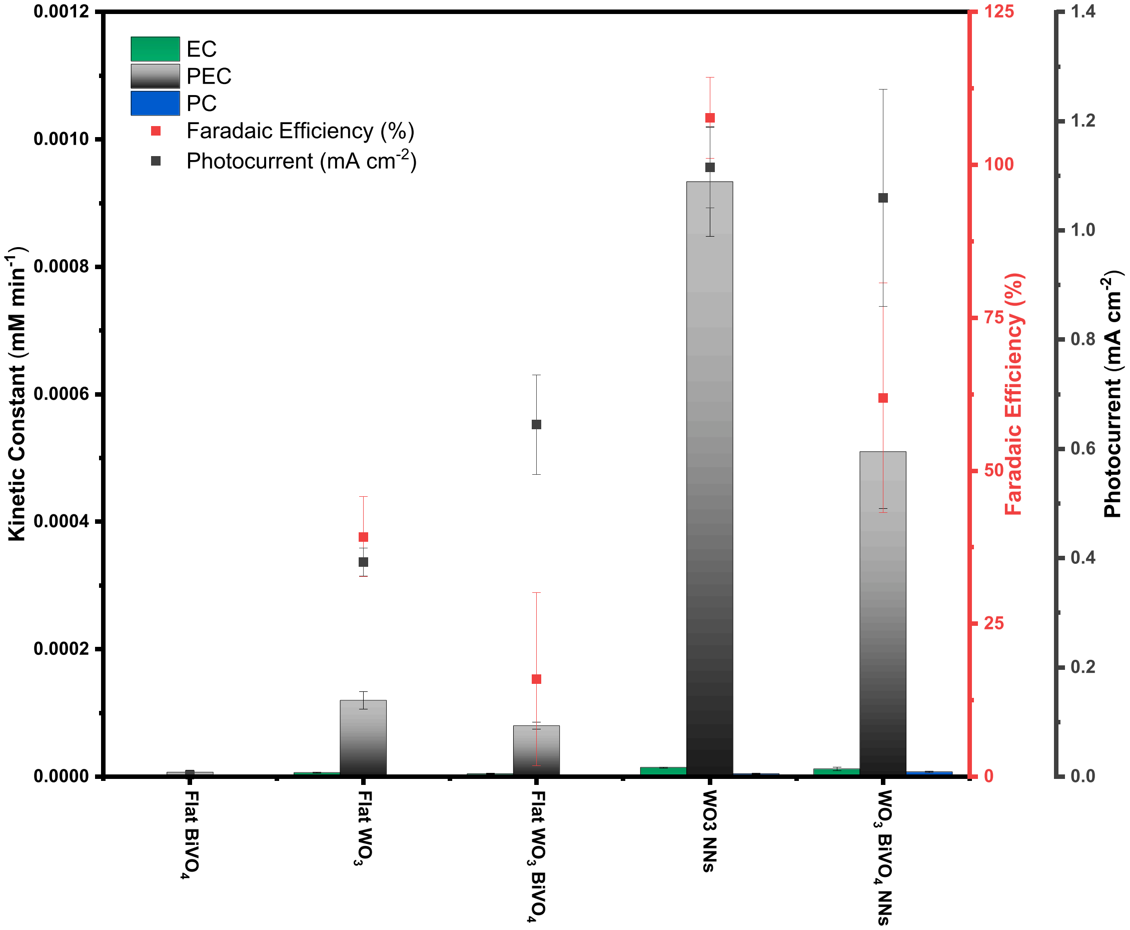

Fig. 2. Comparison of the oxidation of methanol to formaldehyde kinetic constants using photoelectrocatalytic (PEC), electrocatalytic (EC), and photocatalytic (PC) conditions. Table S1 in the Supplementary Information gives the numerical value of all rate constants. In all experiments, a 0.1 M Na_2SO_4 solution was used as electrolyte with an initial concentration of MeOH of 0.1 M. A 365 nm LED light was used for the PEC and PC experiments under back lit conditions. An applied voltage of 0.5 V vs Ag/ AgCl was used for the PEC and EC experiments.

observed trends in the kinetic constants for MeOH oxidation to formaldehyde.

This effect is mainly due to the degradation mechanism of methanol, where hydroxyl groups play an important role in the oxidation of MeOH to formaldehyde. The diffusion paths for hydroxyl radicals are shorter in nanostructured materials. However, nanostructured $WO_3/BiVO_4$ heterojunctions present a lower rate of generation of hydroxyl radicals due to the promotion of electrons from the $BiVO_4$ layer [44]. Therefore, pristine nanostructured WO_3 showed higher rates for the degradation of MeOH followed by its heterojunction analogue.

3.3. Evaluation of the MS2 inactivation efficiency

The antiviral efficiency of the photocatalytic materials studied in this work was evaluated through the inactivation of the MS2 bacteriophage. MS2 concentration *versus* time plots for the five photoanodes are shown in Supplementary Information (Figure S6). These antiviral properties were examined under PEC, EC, and PC conditions. The inactivation of MS2 can be fitted to a pseudo- first order kinetic expression using the gradient of the slope of the log inactivation of MS2 versus time [45]. PEC conditions showed higher efficiency by nearly one order of magnitude (Fig. 3). Interestingly, PEC inactivation of MS2 showed more comparable inactivation rates for flat (WO_3 and $WO_3/BiVO_4$) photoanodes, with a 4-log (99.99 %) inactivation within 5 min, and nanostructured (WO_3 and $WO_3/BiVO_4$) photoanodes, with a 5-log (99.999 %) inactivation within 5 min than was observed for the methanol oxidation. Comparing the respective flat and nanostructured materials, the kinetic constants for MS2 inactivation for the nanostructured materials was only 30–40 % higher than their flat equivalents (Fig. 3), whereas for MeOH this value was closer to 10 times larger (Fig. 2). This may be due to the near 40-fold difference in size between MeOH and MS2. MeOH has an effective diameter of ~0.6 nm, whilst MS2 has a diameter of ~23 nm, therefore, MeOH will likely be able to better penetrate the gaps between nanostructures. Thus, the larger surface area afforded by the nanostructured materials is less beneficial to MS2 than it is to MeOH. Notably, all WO_3 containing samples studied herein showed high MS2 inactivation rates, irrespective of material geometry.

It has been shown in the literature that the inactivation of MS2 is mainly associated with surface generated hydroxyl radicals and some direct oxidation at holes [15]. The negatively charged capsid of MS2 is electrostatically attracted to the positively charged photoanode surface, thus improving the oxidation pathway of MS2 by $^{\bullet}OH$. The generation of $^{\bullet}OH$ is typically slower on $BiVO_4$ than WO_3 photocatalysts, with water oxidation on $BiVO_4$ progressing via multiple proton-couple electron transfer reaction pathways [46]. Furthermore, WO_3 materials have a valence band of 3.1 eV at pH 0, whilst $BiVO_4$ has a valence band of 2.4 eV at pH 0 [36]. The overpotential required to produce $^{\bullet}OH$ from water is 2.7 eV at pH 0 [37], indicating that WO_3 would be expected to generate more $^{\bullet}OH$ under the same conditions, and may explain why all the WO_3 containing materials studied herein displayed high MS2 inactivation rates.

Tolosana-Moranchel *et al.* achieved high photoelectrocatalytic inactivation rates of MS2 using similar materials. The time taken to reach 5- log (99.999 %) inactivation by WO_3 photoanodes tested by

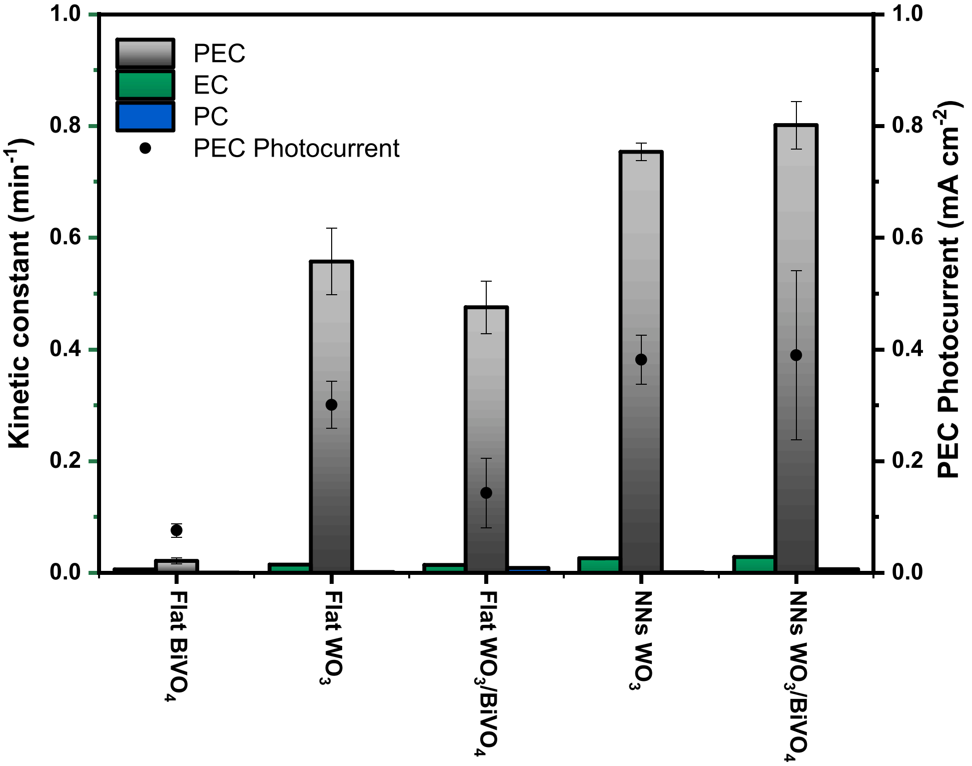

Fig. 3. Kinetic constants of the photoelectrocatalytic (grey bars), electrocatalytic (green bars), and photocatalytic (blue bars) inactivation of MS2 bacteriophage. Table S1 in the Supplementary Information gives the numerical value of all rate constants. In all experiments, a 0.1 M Na_2SO_4 solution was used as electrolyte. A 365 nm LED light was used for the photoelectrocatalytic and photocatalytic experiments under back lit conditions. An applied voltage of 0.5 V vs Ag/ AgCl was used for the photoelectrocatalytic and electrocatalytic experiments.

Tolosana-Moranchel *et al.* was 6 min (0.89 min^{-1}) [18], whilst the kinetic constant observed in this work for nanostructured $WO_3/BiVO_4$ was 0.80 min^{-1} (4.0- log (99.99 %) reduction after 5 min) and 0.75 min^{-1} (3.84- log (99.986 %) reduction after 5 min) for WO_3 in nanostructured form. The work in this publication uses a higher light intensity and a lower potential bias than the tests conducted by Tolosana-Moranchel *et al.*, which could account for the slightly lower kinetic constants observed in this work as higher potential biases would be expected to improve inactivation rates due to greater electrostatic attraction, lower electron-hole recombination, and the subsequent increased rate of generation of ROS.

3.4. Incident photon to current efficiency

The incidence photon to current efficiency (IPCE) of the photoanodes was calculated using chronoamperometric data from the MS2 inactivation and MeOH oxidation experiments and shown in Fig. 4.

$$IPCE(\%) = \frac{I_{pc}}{e}\frac{c}{P_{in}}\frac{h}{\lambda} \tag{2}$$

Where, I_{pc} is the measured photocurrent, c is the speed of light, h is Planck's constant, e is the elementary charge, P_{in} is the light power and λ is the wavelength.

The highest IPCE value for MS2 inactivation was observed using the flat $WO_3/BiVO_4$ photoanode, where the WO_3 layer allowed for greater transmission of photons to the $BiVO_4$, as well as good electron transport back through the WO_3 to the FTO substrate layer. The increased IPCE of flat $WO_3/BiVO_4$ suggests water oxidation is causing the high photocurrent, as this material did not demonstrate comparatively high MS2 inactivation rates. Although electron transport is improved in nanostructured WO_3 materials [47,48], the layer thickness of the nanostructured WO_3 (shown in Figure S2 of the Supplementary Information)

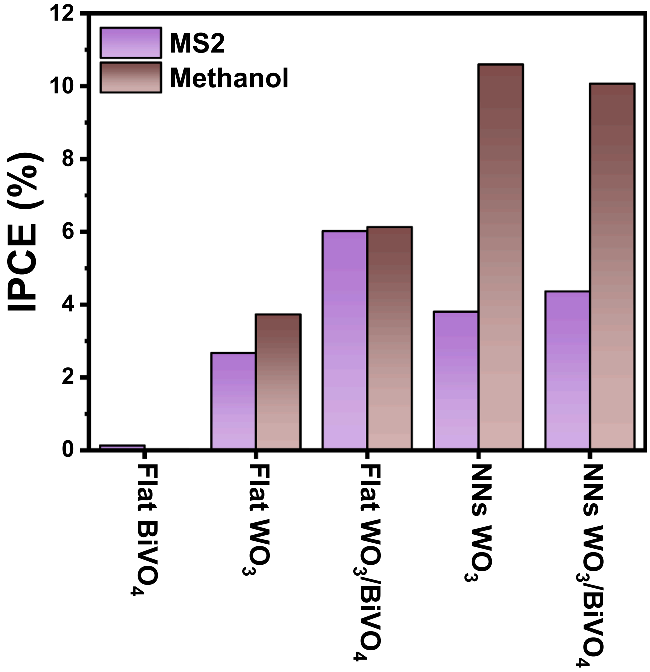

Fig. 4. Incident photon to current efficiency (IPCE), measured at an applied potential of 0.5 V vs Ag/AgCl under back irradiation for the flat (WO_3 and $WO_3/BiVO_4$) and nanostructured (WO_3 and $WO_3/BiVO_4$) photocatalytic materials evaluated in this work. The IPCE values were obtained from the MS2 inactivation and MeOH oxidation experiments.

combined with the quantum confinement effect due to the increased particle size of nanostructured WO_3 reduces the transmission of photons to the outer tips of the WO_3 needles, where the majority of MS2 inactivation will occur [49].

In the case of MeOH oxidation, the nanostructured WO_3 and $WO_3/BiVO_4$ photoanodes displayed higher IPCE values than their flat equivalents. This effect is due to the much larger surface-to-volume ratio of the nanostructured photoanodes compared to their flat analogues, thus the comparatively small MeOH molecule can access sites for oxidation throughout the structure. The current doubling effect of MeOH is evident in the nanostructured photoanodes but not in the flat materials. The absolute IPCE values reported in this work are lower than in other publications of the same materials [18]. This is largely due to the low potential bias (0.5 V *vs* Ag/AgCl) applied to the photoanodes in the experiments to negate the electroosmotic repulsion of negatively charged *E. coli* and MS2 with increasing potential [15,16]. *E. coli* K12 was omitted from IPCE calculations, as the lower light intensity used compared to the other pollutants would not allow for drawing comparisons between all three pollutants as the effect of light intensity on photocatalytic kinetic constants is non-linear [50].

The applied bias photon-to-current efficiency (ABPE) was calculated for methanol oxidation experiments, with the values for the photoanodes shown in Table S2 of the Supplementary Information of this paper and the equation used shown in Eq. S1. The highest ABPE value was observed for the nanostructured materials (NNs WO_3=1.66 %, NNs $WO_3/BiVO_4$=1.57 %), whilst the flat materials had ABPE values less than 1 %.

3.5. Evaluation of the E. coli inactivation efficiency

The antimicrobial performance of the flat and nanostructured photoanodes investigated in this work was evaluated by comparing the kinetic constants for *E. coli* inactivation. These values were calculated using a non-linear regression algorithm to fit the inactivation curves, as previously detailed by some authors of this work [51].

It can be seen in Fig. 5f that the photocatalytic kinetic constants for the inactivation of *E. coli* showed that the flat $WO_3/BiVO_4$ photoanode achieved a similar rate of inactivation compared to its flat analogue and the nanostructured photoanodes. To understand this, the size of an *E. coli* bacterium should be considered. *E. coli* is a rod-shaped body of significantly larger dimensions (diameter of 1 µm and length of 2 µm) than MeOH (~0.6 nm) and MS2 bacteriophage (~23 nm). Therefore, the *E. coli* bacterium can only access the upper most layer of the surface of the photoanode. It has been previously reported that a flat WO_3 coating, with a 100 nm thickness, can absorb 45 % of the photons contained in a light source with a 355 nm wavelength, whilst 15 % are absorbed when the irradiating source presents a 400 nm wavelength [52]. In this work, an LED device with a emission range within 343 – 400 nm and a wavelength peak at 367 nm (Figure S7) was used. The photoanodes explored in this work consisted of flat WO_3 layers with a

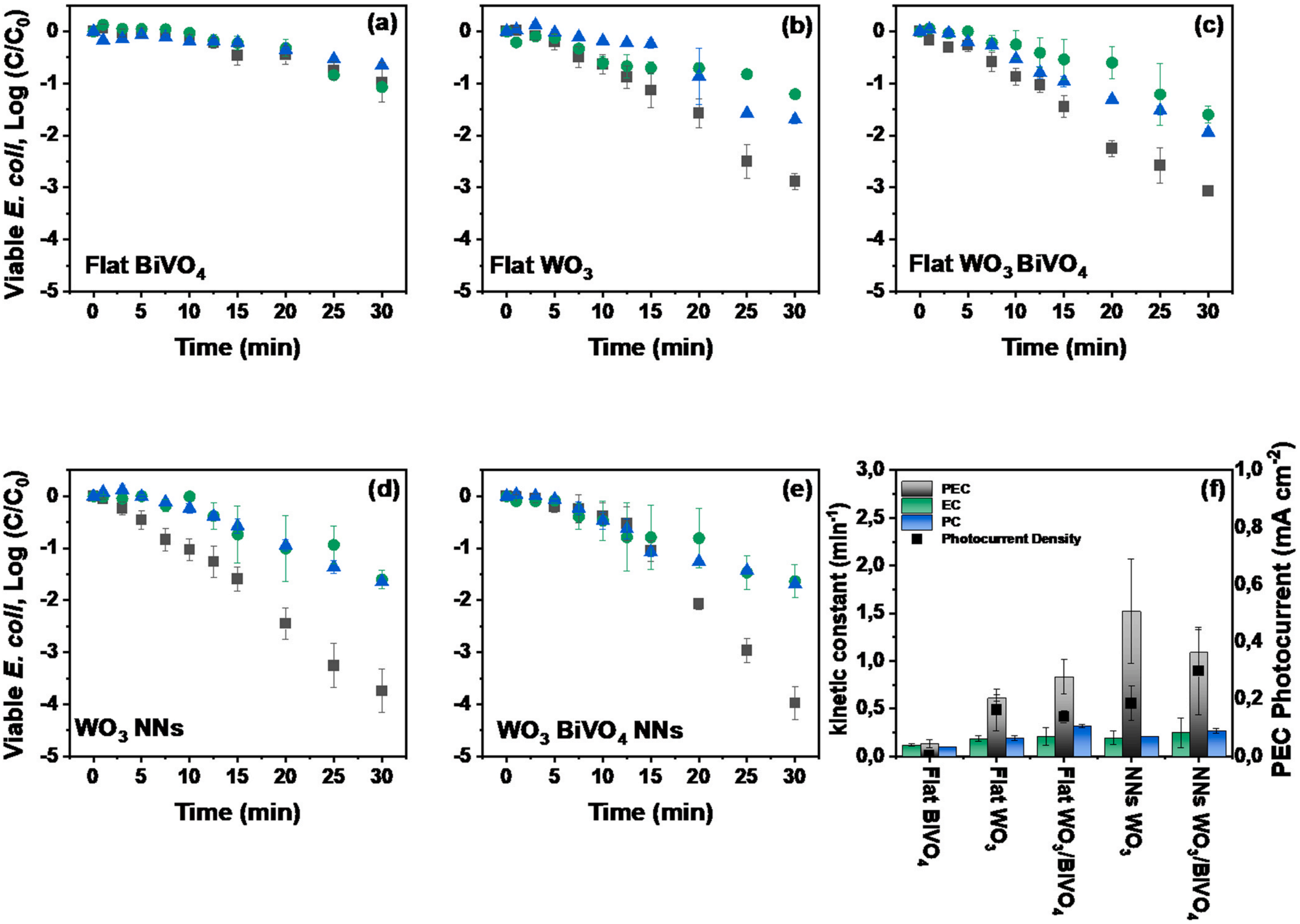

Fig. 5. a-e) Photoelectrocatalytic (grey squares), electrocatalytic (green circles) and photocatalytic (blue triangles) inactivation of *E. coli* K12 (10^6 CFU mL^{-1}, 50 mL). f) Kinetic constants of the photoelectrocatalytic (grey bars), electrocatalytic (green bars), and photocatalytic (blue bars) inactivation of *E. coli* K12. Table S1 in the Supplementary Information gives the numerical value of all rate constants. In all experiments, a 0.1 M Na_2SO_4 solution was used as electrolyte. A UVA LED light (19.1 mW cm^{-2} ± 1.35 mW cm^{-2}) was used for the photoelectrocatalytic and photocatalytic experiments under back lit conditions. An applied voltage of 0.5 V vs Ag/AgCl was used for the photoelectrocatalytic and electrocatalytic experiments. Control experiments shown in Supplementary Information (Fig. S8).

thickness of 90 nm, and nanostructured WO_3 layers with a ~3.3 μm thickness. Therefore, as samples were irradiated from the back, a significant portion of the photons are not absorbed by the $BiVO_4$ layer in heterojunction samples.

PEC inactivation of *E. coli* showed that photoanodes composed of a single layer of nanostructured WO_3 achieved inactivation rates higher than their heterojunction analogues. These results could be attributed to a larger number of hydroxyl radicals being generated in WO_3 photoanodes. Whilst the inactivation of MS2 is largely associated with surface bound $^{\bullet}OH$, *E. coli* inactivation is associated with a wide variety of ROS, including surface and free $^{\bullet}OH$, $O_2^{\bullet}$, H_2O_2 [53], as well as electrolyte-specific oxidants such as sulphate radicals [54]. WO_3 has a deep valence band associated with the generation of $^{\bullet}OH$ radicals. However, $BiVO_4$ has band positions able to generate other ROS, such as H_2O_2 and $O_2^{\bullet}$ [55]. Nevertheless, $^{\bullet}OH$ has the strongest oxidising potential of the radicals generated by each material. As previously mentioned, nanostructured WO_3 exhibited the highest MeOH oxidation rate under PEC conditions, which is an indication of high h^+ and $^{\bullet}OH$ generation. It has been shown that H_2O_2 is generated in photoelectrocatalytic WO_3 systems but is unlikely to be the primary ROS responsible for *E. coli* inactivation. This was demonstrated by isolating the generation of H_2O_2 at the cathode and measuring the inactivation of *E. coli*, which was negligible over the duration of the experiment [56]. The authors suggested *E. coli* inactivation was associated with h^+ generation at the anode. These findings are supported by the poor performance shown by flat $BiVO_4$ photoanodes, which displayed only a 1- log (90 %) reduction after 30 min for *E. coli* inactivation tests. These results indicate that other ROS may be generated by flat $BiVO_4$, such as H_2O_2 and $O_2^{\bullet}$, which can inactivate *E. coli*, but are less effective at oxidising MS2. Another explanation for the lower activity of the flat and nanostructured $WO_3/BiVO_4$ photoanodes compared to nanostructured WO_3 could be the formation of an electroosmotic layer. $WO_3/BiVO_4$ heterojunctions led into a high concentration of holes in the $BiVO_4$ layer. The SO_4^{2-} ions are attracted to the holes on the $BiVO_4$ layer, forming an osmotic barrier for the *E. coli* to access sites for inactivation, as observed in previous works [15,16]. In the case of MS2, the smaller size allows for faster diffusion through the osmotic barrier than *E. coli*, thus is not negatively impacted by the high concentration of ions. Another consideration for the poor performance of the nanostructured $WO_3/BiVO_4$ compared to nanostructured WO_3 is the charge carrier recombination due to hole decay under UVA radiation. Grigioni *et al.* demonstrated that whilst the lifetime of photogenerated holes is improved in $WO_3/BiVO_4$ systems compared to WO_3 in the visible range (470 nm), at 387 nm the incorporation of $BiVO_4$ increased hole decay and charge carrier recombination, which could further explain the poor performance of the heterojunction materials compared to WO_3 alone [57].

4. Conclusions

This work explores the use of nanostructured WO_3-based photocatalysts for water disinfection applications using different electrochemical and photocatalytic conditions. Under photoelectrochemical (PEC) conditions, all nanostructured WO_3-containing materials exhibited high rates of inactivation for MS2, *E. coli*, and MeOH oxidation, highlighting their potential for water disinfection applications. This enhanced performance can be attributed to increased photon absorption, active surface area, and improved charge carrier diffusion, although some challenges, such as charge carrier recombination and electroosmotic effects, were observed.

In addition, incident photon to current efficiency (IPCE) showed enhanced performance for nanostructured materials due to their larger surface-to-volume ratio. This work provides valuable insights into the design and optimisation of photocatalytic materials for efficient water disinfection, paving the way for developing multifunctional materials capable of addressing both water treatment and energy storage challenges.

CRediT authorship contribution statement

Javier Marugan: Writing – review & editing, Validation, Supervision, Methodology, Funding acquisition, Formal analysis, Conceptualization. **Cristina Pablos:** Writing – review & editing, Validation, Supervision, Methodology, Formal analysis, Conceptualization. **Anna Hankin:** Writing – review & editing. **George Creasey:** Writing – review & editing, Investigation. **Carlos Sotelo-Vazquez:** Writing – review & editing, Validation, Methodology, Investigation, Formal analysis, Data curation. **Conor Reddick:** Writing – original draft, Methodology, Investigation. **Simon Stanley:** Writing – review & editing, Validation, Supervision, Formal analysis, Conceptualization. **Ken Reynolds:** Writing – review & editing, Validation, Supervision, Formal analysis, Conceptualization. **Andreas Kafizas:** Writing – review & editing, Validation, Methodology, Formal analysis, Data curation. **Brian Tam:** Writing – review & editing, Validation, Methodology, Formal analysis, Data curation.

Declaration of Competing Interest

The authors declare that they have no known competing financial interests or personal relationships that could have appeared to influence the work reported in this paper.

Data availability

Data will be made available on request.

Acknowledgements

The authors acknowledge the financial support of the European Union's Horizon 2020 Research and Innovation Programme in the frame of REWATERGY, Sustainable Reactor Engineering for Applications on the Water-Energy Nexus, MSCA-ITN-EID Project N. 812574. C. S.-V. would like to thank the Regional Government of Madrid for financial support through Programa de Atracción de Talento (2019-T2/AMB-13122) and the Young Researchers R&D Project (Bio-PhLoW) financed by Regional Government of Madrid and Rey Juan Carlos University.

This Special Issue is dedicated to honor the retirement of Prof. Santiago Esplugas at the Universitat de Barcelona (UB, Spain), a key figure in the area of Catalytic Advanced Oxidation Processes that has significantly influenced the research and vision of AOP.

Appendix A. Supporting information

Supplementary data associated with this article can be found in the online version at doi:10.1016/j.cattod.2024.114783.

References

[1] Paul, D., Kolar, P. & Hall, S.G. A Review of the Impact of Environmental Factors on the Fate and Transport of Coronaviruses in Aqueous Environments. doi:10.1038/s41545-020-00096-w.

[2] S.D. Richardson, Disinfection by-products and other emerging contaminants in drinking water, TrAC Trends Anal. Chem. 22 (2003) 666–684.

[3] L.A. Galeano, M. Guerrero-Flórez, C.A. Sánchez, A. Gil, M.Á. Vicente, Disinfection by chemical oxidation methods, Handb. Environ. Chem. 67 (2019) 257–295.

[4] J. Gomes, D. Frasson, R.M. Quinta-Ferreira, A. Matos, R.C. Martins, Removal of enteric pathogens from real wastewater using single and catalytic ozonation, Water 11 (2019) 127.

[5] S. Giannakis, S. Liu, A. Carratalà, S. Rtimi, M. Bensimon, C. Pulgarin, Effect of Fe(II)/Fe(III) species, pH, irradiance and bacterial presence on viral inactivation in wastewater by the photo-Fenton process: Kinetic modeling and mechanistic interpretation, Appl. Catal. B Environ. 204 (2017) 156–166.

[6] S. Corby, E. Pastor, Y. Dong, X. Zheng, L. Francàs, M. Sachs, S. Selim, A. Kafizas, A. A. Bakulin, J.R. Durrant, Charge separation, band-bending, and recombination in WO3 photoanodes, J. Phys. Chem. Lett. 10 (2019) 5395–5401.

[7] D.O. Scanlon, et al., Band alignment of rutile and anatase TiO2, Nat. Mater. 129 (12) (2013) 798–801.

[8] R. Quesada-Cabrera, C. Sotelo-Vazquez, J.C. Bear, J.A. Darr, I.P. Parkin, R. Quesada-Cabrera, C. Sotelo-Vazquez, J.C. Bear, J.A. Darr, I.P. Parkin, Photocatalytic evidence of the rutile-to-anatase electron transfer in Titania, Adv. Mater. Interfaces 1 (2014) 1400069.

[9] S.J.A. Moniz, S.A. Shevlin, D.J. Martin, Z.X. Guo, J. Tang, Visible-light driven heterojunction photocatalysts for water splitting – a critical review, Energy Environ. Sci. 8 (2015) 731–759.

[10] M. Anaya, B.P. Rand, R.J. Holmes, D. Credgington, H.J. Bolink, R.H. Friend, J. Wang, N.C. Greenham, S.D. Stranks, Best practices for measuring emerging light-emitting diode technologies, Nat. Photonics 13 (2019) 818–821.

[11] H. Wang, L. Zhang, Z. Chen, J. Hu, S. Li, Z. Wang, J. Liu, X. Wang, Semiconductor heterojunction photocatalysts: design, construction, and photocatalytic performances, Chem. Soc. Rev. 43 (2014) 5234–5244.

[12] C. Nomellini, A. Polo, C.A. Mesa, E. Pastor, G. Marra, I. Grigioni, M.V. Dozzi, S. Giménez, E. Selli, Improved Photoelectrochemical Performance of WO3/BiVO4 Heterojunction Photoanodes via WO3 Nanostructuring, ACS Appl. Mater. Interfaces 15 (2023) 52436–52447.

[13] Z. Sun, J.H. Kim, Y. Zhao, F. Bijarbooneh, V. Malgras, Y. Lee, Y.M. Kang, S.X. Dou, Rational design of 3D dendritic TiO2 nanostructures with favorable architectures, J. Am. Chem. Soc. 133 (2011) 19314–19317.

[14] J.H. Bang, P.V. Kamat, Solar cells by design: photoelectrochemistry of TiO2 nanorod arrays decorated with CdSe, Adv. Funct. Mater. 20 (2010) 1970–1976.

[15] M. Cho, E.L. Cates, J.H. Kim, Inactivation and surface interactions of MS-2 bacteriophage in a TiO2 photoelectrocatalytic reactor, Water Res 45 (2011) 2104–2110.

[16] S. McMichael, A. Tolosana-Moranchel, M.A.L.R.M. Cortes, J.W.J. Hamilton, P. Fernandez-Ibanez, J.A. Byrne, An investigation of photoelectrocatalytic disinfection of water using titania nanotube photoanodes with carbon cathodes and determination of the radicals produced, Appl. Catal. B Environ. 311 (2022) 121339.

[17] N. Baram, D. Starosvetsky, J. Starosvetsky, M. Epshtein, R. Armon, Y. Ein-Eli, Enhanced inactivation of E. coli bacteria using immobilized porous TiO2 photoelectrocatalysis, Electrochim. Acta 54 (2009) 3381–3386.

[18] A. Tolosana-Moranchel, N. Pichel, H. Lubarsky, J.A. Byrne, P. Fernández-Ibañez, Photoelectrocatalytic degradation of pharmaceuticals and inactivation of viruses in water with tungsten oxide electrodes, J. Environ. Chem. Eng. 10 (2022) 107955.

[19] E. Scott-Emuakpor, G.I. Paton, M.J. Todd, D.E. Macphee, Disinfection of E. coli contaminated water using tungsten trioxide-based photoelectrocatalysis, Environ. Eng. Manag. J. 15 (2016) 899–903.

[20] Pihosh, Y. *et al.* Photocatalytic generation of hydrogen by core-shell WO3/BiVO4 nanorods with ultimate water splitting efficiency, Sci. Rep., 2015 51 5, 1–10 (2015).

[21] V. Cristino, et al., Photoelectrocatalytic degradation of emerging contaminants at WO3/BiVO4 photoanodes in aqueous solution, Photochem. Photobiol. Sci. 18 (2019) 2150–2163.

[22] N. Omrani, A. Nezamzadeh-Ejhieh, BiVO4/WO3 nano-composite: characterization and designing the experiments in photodegradation of sulfasalazine, Environ. Sci. Pollut. Res. 27 (2020) 44292–44305.

[23] A. Kafizas, L. Francàs, C. Sotelo-Vazquez, M. Ling, Y. Li, E. Glover, L. McCafferty, C. Blackman, J. Darr, I. Parkin, Optimizing the activity of nanoneedle structured WO3 photoanodes for solar water splitting: direct synthesis via chemical vapor deposition, J. Phys. Chem. C 121 (2017) 5983–5993.

[24] C. Reddick, C. Casado, K. Reynolds, S. Stanley, C. Pablos, J. Marugán, Evaluation of the uniformity of UVA LED illumination on flat surfaces: discrete ordinate method, single axis, and surface scanning radiometry, Heliyon 9 (2023).

[25] T. NASH, The colorimetric estimation of formaldehyde by means of the Hantzsch reaction, Biochem. J. 55 (1953) 416.

[26] M. Martín-Sómer, D. Benz, J.R. van Ommen, J. Marugán, Multitarget evaluation of the photocatalytic activity of P25-SiO2 prepared by atomic layer deposition, Catalysts 10 (2020), https://doi.org/10.3390/catal10040450.

[27] C. Pablos, J. Marugán, R. Van Grieken, C. Adán, A. Riquelme, J. Palma, Correlation between photoelectrochemical behaviour and photoelectrocatalytic activity and scaling-up of P25-TiO2 electrodes, Electrochim. Acta (2014), https://doi.org/10.1016/j.electacta.2014.03.038.

[28] E. Kalamaras, P. Lianos, Current Doubling effect revisited: current multiplication in a PhotoFuelCell, J. Electroanal. Chem. 751 (2015) 37–42.

[29] J. Lee, T. Kato, A. Fujishima, K. Honda, Photoelectrochemical oxidation of alcohols on polycrystalline zinc oxide, Bull. Chem. Soc. Jpn. 57 (1984) 1179–1183.

[30] C.A. Mesa, A. Kafizas, L. Francàs, S.R. Pendlebury, E. Pastor, Y. Ma, F. Le Formal, M.T. Mayer, M. Grätzel, J.R. Durrant, Kinetics of photoelectrochemical oxidation of methanol on hematite photoanodes, J. Am. Chem. Soc. 139 (2017) 11537–11543.

[31] A.A. Wilson, S. Corby, L. Francàs, J.R. Durrant, A. Kafizas, The effect of nanoparticulate PdO co-catalysts on the faradaic and light conversion efficiency of WO 3 photoanodes for water oxidation, Phys. Chem. Chem. Phys. 23 (2021) 1285–1291.

[32] R.àfols I. Bellés, C. Selim, S. Harrison, N.M. Ahmad, E.A. Kafizas, A. Beyond band bending in the WO3/BiVO4 heterojunction: insight from DFT and experiment, Sustaion. Energy Fuels 3 (2018) 264–271.

[33] L. Steier, I. Herraiz-Cardona, S. Gimenez, F. Fabregat-Santiago, J. Bisquert, S. D. Tilley, M. Grätzel, Understanding the role of underlayers and overlayers in thin film hematite photoanodes, Adv. Funct. Mater. 24 (2014) 7681–7688.

[34] Y. Liang, T. Tsubota, L.P.A. Mooij, R. van de Krol, Highly improved quantum efficiencies for thin film BiVO4 photoanodes, J. Phys. Chem. C 115 (2011) 17594–17598.

[35] H. Kim, H.Y. Yoo, S. Hong, S. Lee, S. Lee, B.S. Park, H. Park, C. Lee, J. Lee, Effects of inorganic oxidants on kinetics and mechanisms of WO3-mediated photocatalytic degradation, Appl. Catal. B Environ. 162 (2015) 515–523.

[36] J. Zhang, Y. Nosaka, Generation of OH radicals and oxidation mechanism in photocatalysis of WO3 and BiVO4 powders, J. Photochem. Photobiol. A Chem. 303–304 (2015) 53–58.

[37] G.V. Buxton, C.L. Greenstock, W.P. Helman, A.B. Ross, Critical Review of rate constants for reactions of hydrated electrons, hydrogen atoms and hydroxyl radicals (·OH/·O− in Aqueous Solution, J. Phys. Chem. Ref. Data 17 (2009) 513.

[38] C.C.L. McCrory, S. Jung, J.C. Peters, T.F. Jaramillo, Benchmarking heterogeneous electrocatalysts for the oxygen evolution reaction, J. Am. Chem. Soc. 135 (2013) 16977–16987.

[39] Y. Ma, A. Kafizas, S.R. Pendlebury, F. Le Formal, J.R. Durrant, Photoinduced absorption spectroscopy of CoPi on BiVO4: the function of CoPi during water oxidation, Adv. Funct. Mater. 26 (2016) 4951–4960.

[40] M. Yin, C. Liu, R. Ge, Y. Fang, J. Wei, X. Chen, Q. Chen, X. Chen, Paper-supported near-infrared-light-triggered photoelectrochemical platform for monitoring Escherichia coli O157:H7 based on silver nanoparticles-sensitized-upconversion nanophosphors, Biosens. Bioelectron. (203, () (2022).

[41] S. Sheik Mydeen, R. Raj Kumar, M. Kottaisamy, V.S. Vasantha, Biosynthesis of ZnO nanoparticles through extract from Prosopis juliflora plant leaf: antibacterial activities and a new approach by rust-induced photocatalysis, J. Saudi Chem. Soc. 24 (2020) 393–406.

[42] F.F. Abdi, T.J. Savenije, M.M. May, B. Dam, R. van de Krol, The origin of slow carrier transport in BiVO4 thin film photoanodes: a time-resolved microwave conductivity study, J. Phys. Chem. Lett. 4 (2013) 2752–2757.

[43] B.R. Lee, M.G. Lee, H. Park, T.H. Lee, S.A. Lee, S.S.M. Bhat, C. Kim, S. Lee, H. W. Jang, All-solution-processed WO3/BiVO4 core-shell nanorod arrays for highly stable photoanodes, ACS Appl. Mater. Interfaces 11 (2019) 20004–20012.

[44] J. Liu, W. Chen, Q. Sun, Y. Zhang, X. Li, J. Wang, C. Wang, Y. Yu, L. Wang, X. Yu, Oxygen vacancies enhanced WO3/BiVO4Photoanodes modified by cobalt phosphate for efficient photoelectrochemical water splitting, ACS Appl. Energy Mater. 4 (2021) 2864–2872.

[45] D. Venieri, I. Gounaki, V. Binas, A. Zachopoulos, G. Kiriakidis, D. Mantzavinos, Inactivation of MS2 coliphage in sewage by solar photocatalysis using metal-doped TiO2, Appl. Catal. B Environ. 178 (2015) 54–64.

[46] T. Saison, N. Chemin, C. Chanéac, O. Durupthy, L. Mariey, F. Maugé, V. Brezová, J. P. Jolivet, New insights into BiVO4 properties as visible light photocatalyst, J. Phys. Chem. C 119 (2015) 12967–12977.

[47] Y. Chai, C.W. Tam, K.P. Beh, F.K. Yam, Z. Hassan, Effects of thermal treatment on the anodic growth of tungsten oxide films, Thin Solid Films 588 (2015) 44–49.

[48] T. Zhu, M.N. Chong, Y.W. Phuan, E.S. Chan, Electrochemically synthesized tungsten trioxide nanostructures for photoelectrochemical water splitting: influence of heat treatment on physicochemical properties, photocurrent densities and electron shuttling, Colloids Surf. A Physicochem. Eng. Asp. 484 (2015) 297–303.

[49] Houweling, Z. S., Harks, P. P. R. M. L., Kuang, Y., Van Der Werf, C. H. M., Geus, J. W. & Schropp, R. E. I, Hetero- and homogeneous three-dimensional hierarchical tungsten oxide nanostructures by hot-wire chemical vapor deposition, Thin Solid Films 575 (2015) 76–83.

[50] J.M. Herrmann, Photocatalysis fundamentals revisited to avoid several misconceptions, Appl. Catal. B Environ. 99 (2010) 461–468.

[51] J. Marugán, R. van Grieken, C. Sordo, C. Cruz, Kinetics of the photocatalytic disinfection of Escherichia coli suspensions, Appl. Catal. B Environ. 82 (2008) 27–36.

[52] I. Ràfols, C. Bellés, S. Selim, N.M. Harrison, E.A. Ahmad, A. Kafizas, Beyond band bending in the WO 3 /BiVO 4 heterojunction: insight from DFT and experiment. *Sustain*, Energy Fuels 3 (2018) 264–271.

[53] M. Cho, H. Chung, W. Choi, J. Yoon, Different inactivation behaviors of MS-2 phage and Escherichia coli in TiO2 photocatalytic disinfection, Appl. Environ. Microbiol. 71 (2005) 270–275.

[54] A. Ahmadi, T. Wu, Inactivation of E. coli using a novel TiO2 nanotube electrode, Environ. Sci. Water Res. Technol. 3 (2017) 534–545.

[55] M. Nishikawa, S. Hiura, Y. Mitani, Y. Nosaka, Enhanced photocatalytic activity of BiVO4 by co-grafting of metal ions and combining with CuBi2O4, J. Photochem. Photobiol. A Chem. 262 (2013) 52–56.

[56] I. Salmerón, P.K. Sharma, M.I. Polo-López, A. Tolosana, S. McMichael, I. Oller, J. A. Byrne, P. Fernández-Ibáñez, Electrochemically assisted photocatalysis for the simultaneous degradation of organic micro-contaminants and inactivation of microorganisms in water, Process Saf. Environ. Prot. 147 (2021) 488–496.

[57] I. Grigioni, K.G. Stamplecoskie, D.H. Jara, M.V. Dozzi, A. Oriana, G. Cerullo, P. V. Kamat, E. Selli, Wavelength-dependent ultrafast charge carrier separation in the WO3/BiVO4 coupled system, ACS Energy Lett. 2 (2017) 1362–1367.